Numerical assessment of triply periodic minimal surfaces for direct air capture of carbon dioxide

Kellis Kincaid[a,*], Filipe L. Brandao[a], Flavio D. F. Chuahy[a] and Kashif Nawaz[a]

[a]Oak Ridge National Laboratory, 1 Bethel Valley Road, Oak Ridge, Tennessee, 37830, USA

ARTICLE INFO

Keywords:
triply periodic
gyroid
carbon
DAC
CFD

ABSTRACT

Direct air capture (DAC) systems often consist of packing material wetted by a capture fluid that reacts with CO_2 in the airstream. The efficiency of the contactor is determined by a complex relationship of fluid dynamics, heat and mass transfer, contactor geometry, and chemical properties. The efficiency of the contactor must be balanced with other factors, primarily pressure drop through the system. Triply periodic minimal surfaces (TPMS) are a class of differential surfaces that have been explored in multiple engineering applications and have been shown to exhibit excellent performance when used in heat exchangers. Their tortuous path provides a high surface-to-volume ratio and favorable trade-off between contact area and pressure drop. In this work, a gyroid-type TPMS contactor was evaluated using computational fluid dynamics for a variety of geometric parameters to explore the potential benefit of TPMS shapes for DAC applications. A thin-film model was employed to model the flow and distribution of the capture solvent, allowing efficient simulations of TPMS structures at scale by eliminating the need for a computationally intensive interface capturing method. A liquid-gas mass transfer model was implemented in the commercial software STAR-CCM+ and used to predict the CO_2 capture efficiency and study the trade-off between capture performance and pressure drop through analysis of capture rates, mass transfer coefficients, and other relevant variables. TPMS contactors with a variety of geometric parameters and two capture solvent options were investigated to determine the effect of design choices on the operational performance of DAC systems. Results showed that while contactor geometry is the dominant factor in efficiency and pressure drop, the physiochemical properties of the solvent are an important secondary influence on the contactor performance.

1. Introduction

The most recent Intergovernmental Panel on Climate Change (IPCC) sixth assessment report (AR6) states that reaching net-zero greenhouse gas (GHG) emissions not only requires significant reductions in CO_2, CH_4, and other GHG emissions, but also active removal of CO_2 from the atmosphere. One of the main forms of carbon dioxide removal, carbon capture, is a process in which CO_2 is separated from a gaseous mixture such as the atmosphere or an exhaust stream. This process can be broadly divided into two categories: point source capture (PSC), in which CO_2 is directly separated from combustion or other process waste streams with high concentrations of CO_2 and sent to storage, and direct air capture (DAC), in which CO_2 is removed from the atmosphere. DAC presents a larger technical challenge than PSC, largely because the concentration of carbon dioxide in the atmosphere (currently around 0.04%) is orders of magnitude larger than typical exhaust gas streams (often 8-14%). Such a low concentration reduces the rate of mass transfer from the gas mixture to the capture solvent, which limits the overall capture efficiency of the system.

DAC systems consist of a coupled series of subsystems, beginning with a contactor, where a gaseous mixture containing CO_2 is brought into contact with a liquid containing a chemical solvent which absorbs and reacts with CO_2. The by-products of this reaction are sent through a complex cycle of processing and regeneration, which requires substantial

*Corresponding author
kincaidkc@ornl.gov (K. Kincaid)
https://www.ornl.gov/staff-profile/kellis-c-kincaid (K. Kincaid)
ORCID(s): 0000-0002-9828-0201 (K. Kincaid)

thermal energy input. Although significant research has been devoted to each stage of the DAC system, overall process efficiency remains low and costs remain high, limiting widespread commercial and industrial adoption. To encourage more widespread use, the capture efficiency of DAC systems must be increased while simultaneously lowering the required energy input.

Contactor performance is typically limited by the competing effects of surface area and pressure drop. High–surface area designs, which have more area for mass transfer to occur, typically result in higher pressure drop because of additional surface drag and obstructions within the flow. Various designs have been proposed to address this issue: packed beds, columnar packings, and other common reactor configurations have achieved moderate success. Triply periodic minimal surfaces (TPMSs) are a new class of reactor designs distinct from previously proposed geometries. These geometries are formed by finding the isosurface of a 3D periodic function and thickening this surface to achieve the desired structural strength and interstitial void size (i.e., porosity). TPMSs are typically classified based on the mathematical forms from which they are derived; two example functions are provided in Table 1, and visualizations of the gyroid type structures used in this work are provided in Figure 1. TPMS shapes are difficult to produce via conventional manufacturing methods due to their geometric complexity; as such, their performance has not yet been fully characterized for a variety of applications. Advances in new manufacturing methods, such as additive manufacturing, have enabled the creation of prototype geometries for research work, and could be used for commercial production as the cost of additively manufactured components continues to decrease. Prototype TPMS structures have demonstrated substantial success in heat exchanger applications. For example, Iyer et al. [1] reported that some TPMS heat exchanger designs can reduce pressure drop by 3 to 10 times while maintaining the same or better performance as traditional shell-in-tube exchangers. Reynolds et al. [2] measured a 13% improvement in the Nusselt number over a straight-tube heat exchanger with the same pumping power. Initial research has also examined the structural integrity of TPMS structures [3], including with functionally graded porosity [4]. Functionally graded contactors such as these have been gaining increased attention in the tissue-engineering research community [5]. Despite these promising initial studies, significant further effort is necessary to optimize TPMS geometries for both heat and mass transfer applications.

Table 1: Mathematical forms of TPMSs

TPMS Type	**Functional Form**
Gyroid	$\sin(x)\cos(y) + \sin(y)\cos(z) + \sin(z)\cos(x) = 0$
Fischer–Koch	$\cos(2x)\sin(y)\cos(z) + \cos(x)\cos(2y)\sin(z) + \sin(x)\cos(y)\cos(2z) = 0$

The properties of TPMS designs are alluring for deployment in DAC contactors. Design and operation of the contactor stage are some of the most important elements of overall system efficiency. Additionally, the contactor stage can represent as much as 27% of the required capital expenditure of a CO_2 absorber system, and approximately 20% of its operating cost [7]. While these costs comprise only a fraction of the total DAC system cost, major improvements in the performance of the contactor stage could result in appreciable reductions in DAC system capital and operating costs. Towards this end, geometric and operational choices should be made to yield high gas-to-film interface areas, large absorption rates, and minimal pumping losses, properties inherent to TPMS structures. In recent work, Ellebracht et al. [8] explored the use of TPMS-based packing materials to replace the commonly used Mellapack 250.Y packing. Although their focus was on PSC, in which the stream CO_2 concentration is on the order of 10%, their experimental and simulation results show a substantial increase in mass transfer performance and effective gas–liquid interfacial area for the TPMS packings. These results are in line with the previously mentioned observations of TPMS geometry performance in heat exchangers. In light of these results, it is of interest to explore the use of TPMS-based packing materials for DAC where CO_2 concentrations are much lower and to evaluate the materials' potential benefits through parametric evaluation of their geometry and construction.

Although several small-scale experiments have been reported in the literature for basic contactor designs such as tubes [9], microchannels [10], and packed beds [11, 12], numerical models are more often used to interrogate the performance of new designs, operating points, and other choices. These numerical models range from low-order system models, which predict the performance of not only the contactor but the entire DAC process, to high-fidelity coupled models, which resolve the space- and time-varying flow structures and chemical processes present in the device. Although all

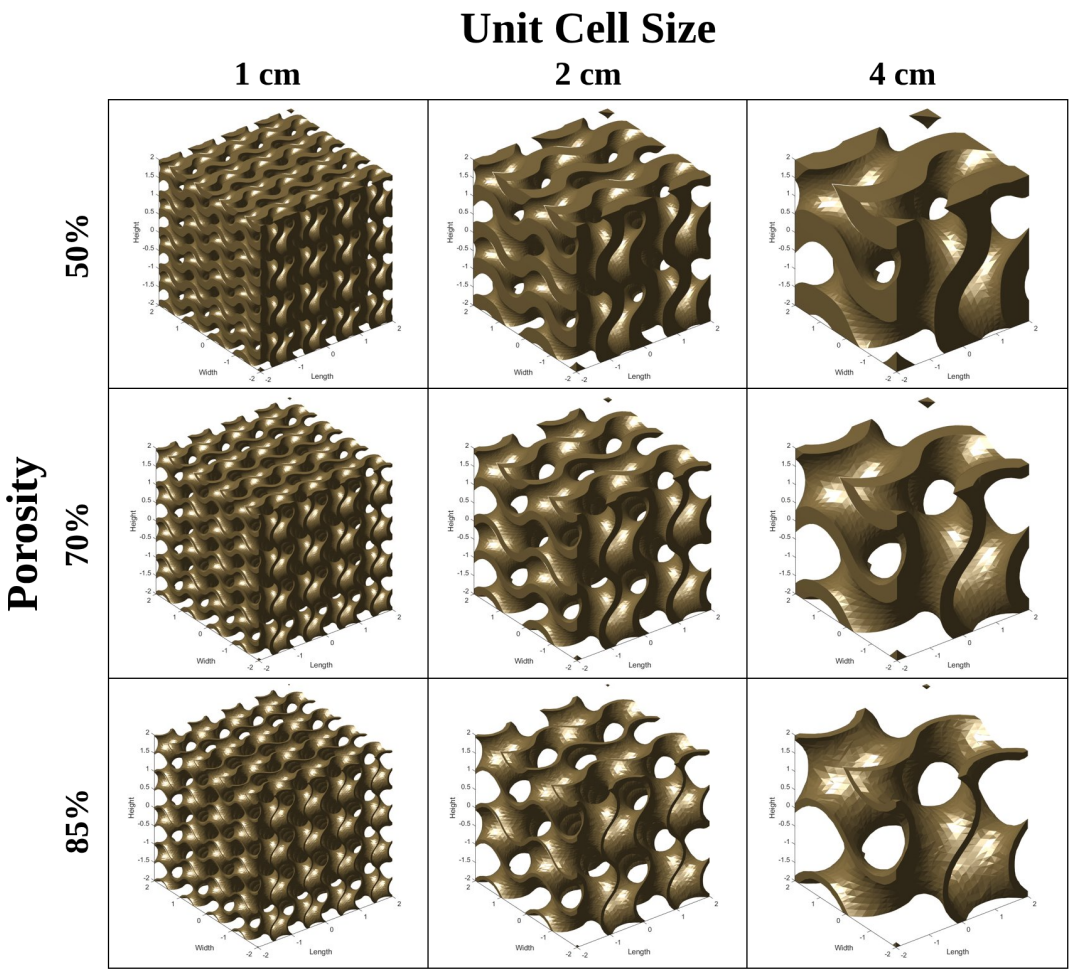

Figure 1: Visualization of gyroid TPMS shapes used in this work (generated with MSLattice [6])

approaches are valid in certain scenarios, each has general guidelines for the problems to which it is most applicable. For instance, low-order system models are often used to probe the design space of well-established configurations. They often require empirical correlations for flow and reaction processes and thus are limited by the availability of these data. However, they can be used with great success when these correlations have been predetermined. One recent example of a successful system-level code was deployed by Ma et al. [13], who conducted a study to optimize a carbon capture system in tandem with a combined heat and power cycle. On a smaller scale, Thompson and Tsouris [14] devised a rate-based model to determine the effects of various additively manufactured packing geometries on the performance of a solvent-based contactor. Although their model required empirical correlations for heat and mass transfer, it demonstrated the performance benefit obtainable by incorporating active cooling channels in AM packings. Reduced-order models are also particularly well suited for coupling with machine learning algorithms because of their low computational expense. These algorithms can be employed to conduct technoeconomic optimization [15, 16], as well as investigate coupling with other energy systems [17].

On the other end of the spectrum, high-fidelity models are often used to probe the physical phenomena underlying contactor performance. At the cost of computational resources, processes such as fluid flow, heat and mass transfer, and chemical reactions are fully resolved to achieve highly accurate predictions of efficiency, pressure drop, and other metrics. As one example, Li et al. [18] published several studies in which they employed a finely resolved model to complete parametric studies of a tube-in-tube microchannel reactor, for which they constructed and validated a

new mass transfer model [19]. In another series of publications, Sebastia-Saez et al. [20, 21, 22] provided another framework for modeling mass transfer between a gas and liquid film. Although such finely resolved models can achieve excellent results, they often employ the volume-of-fluid (VOF) method [23] to resolve the gas–liquid interface, which requires significant mesh refinement around the interface to achieve acceptable results, increasing computation time and limiting the physical size of the problem. As an alternative to the expensive VOF method, Chuahy et al. [24] proposed and validated a novel thin-film modeling approach for DAC applications. This methodology relaxes the constraints on mesh refinement near the gas–liquid interface and allows coarser meshes, and hence larger problems, to be solved. This approach is possible because the low liquid solvent load often used for DAC system operation results in a thin coating of solvent on the system walls, rather than the flooded flow regime often employed in PSC systems, enabling the use of a simplified flow model.

In addition to contactor design, the characteristics of the solvent are important to overall system performance. The solvent choice must balance performance metrics such as absorptivity and reaction kinetics with practical operational considerations such as volatility, corrosivity, and expense. While a variety of solvent types are being considered for carbon capture, aqueous amine solutions are one of the most common choices for DAC systems. Monoethanolamine (MEA), for example, offers high CO_2 reactivity and absorption rates. Other amines like diethanolamine and methyldiethanolamine have also been explored, but offer lower CO_2 loading capacity and slow absorption kinetics [25]. More recently, amino acid salt solvents such as potassium sarcosinate (KSAR) have garnered attention as a superior alternative to conventional amine solvents because of their advantages such as lower volatility and corrosivity [26]. These salts typically dissociate in an aqueous solution, forming an ionic solution which can introduce additional reaction pathways for the absorption of CO_2 and the interaction of reaction products. A number of experimental studies have been conducted to investigate the performance of different solvent types; however, numerical efforts are limited by the availability of complete physiochemical property and reaction kinetics information, which is only available for a few solvent systems.

In this work, the thin-film approach was extended to model a TPMS contactor geometry for the first time. Geometric parameters of the contactor, including TPMS type, unit cell size, porosity, and functional grading were varied, and the resulting effects on performance were noted and their underlying causes examined. In addition, each geometric configuration was tested with two chemical solvents, MEA and KSAR, allowing a detailed comparison of solvent performance. These results will be used to guide future work on contactor design, reducing the need for costly prototyping and allowing for intelligent decisions to be made ahead of construction and testing.

2. Methods

In this section, the equations governing fluid flow and heat transfer are briefly presented, and then the details of the chemical reaction mechanism and mass transfer model are discussed. The equation set was implemented and solved using Siemens Simcenter StarCCM+, version 24.06.

2.1. Conservation Equations

The movement of the capture fluid and gas mixture is governed by the classical incompressible Navier–Stokes equations, which specify the conservation of mass and momentum in each phase.

$$\frac{\partial \rho_i}{\partial t} + \nabla \cdot \left(\rho \vec{u}_i\right) = \dot{m}_i \tag{1}$$

$$\frac{\partial \rho_i \vec{u}_i}{\partial t} + \nabla \cdot \left(\rho_i \vec{u}_i \vec{u}_i\right) = -\nabla p_i + \mu_i \nabla^2 \vec{u}_i + \rho_i \vec{g} \tag{2}$$

Here, the subscript i denotes the phase (liquid or gas), ρ_i is the phase density, t is time, $\vec{u}_i$ is the phase velocity vector, p_i is the phase thermodynamic pressure, μ_i is the phase dynamic viscosity, and $\vec{g}$ is the gravitational vector. The source term $\dot{m}_i$ on the right side of Equation (1) accounts for mass transfer between phases, as detailed further in Section 2.3, and in general has a nonzero value only in cells containing the phase interface.

In addition to mass and momentum, the conservation of energy is required by Equation (3), recast with temperature as the primitive variable.

$$\rho_i c_{p,i} \frac{\partial T_i}{\partial t} + \rho c_{p,i} \vec{u}_i \cdot \nabla T_i = k_i \nabla^2 T_i + \dot{q}_{r,i} \tag{3}$$

Here, $c_{p,i}$ is the specific heat, T_i is the temperature, and k_i is the thermal conductivity. The source term $\dot{q}_{r,i}$ is a result of chemical processes, described further in Section 2.2. At the phase interface, appropriate continuity conditions are imposed for all quantities.

The set of Equations (1)–(3) was solved using a cell-centered finite volume approach in the bulk phase; in the capture fluid phase, however, a thin-film approximation was employed, and the equations were averaged over the film thickness. This procedure reduced the solution to a finite area problem. The thin-film approach was validated by the authors in a previous work [24] and has been shown to yield substantial savings in computational cost and resources compared with a traditional VOF method [23] while maintaining acceptable accuracy for the problem at hand.

2.2. Amino Acid Reaction Mechanism

When dissolved into a solution containing an amino acid, CO_2 reacts to form a number of primary and secondary products. In this work, only the initial reaction of CO_2 to form a primary product was considered because this is the process that reduces the concentration of CO_2 in the film and therefore plays an important role in the overall mass transfer process. In this work, reactions from the common termolecular and base-catalyzed hydration mechanisms were considered. These reactions are applicable to both the MEA and KSAR solvents considered in this work:

$$CO_2(aq) + \mathrm{R} + \mathrm{B} \rightarrow \mathrm{RCOO}^- + \mathrm{B}^+. \tag{4}$$

Here, R represents the amino acid functional group (i.e., MEA or KSAR), and B represents one of two base reactants: either H_2O or a second R functional group. Note that the base product acquires a hydrogen nucleus in this reaction, and the free electron is retained by the amino acid carbamate compound. In this work, the reactions were considered to be second order and irreversible, with a rate described by the reaction coefficient $k_{R,B}$ for a reaction between the amino acid group R and the base B. The following Arrhenius-type reaction rates were used for the MEA [14] and KSAR [27] reaction rates:

$$k_{MEA,MEA} = 4.61 \times 10^9 \exp\left(-4,412/T\right) \ \mathrm{m^6 kmol^{-2} s^{-1}}, \tag{5}$$

$$k_{MEA,H_2O} = 4.55 \times 10^6 \exp\left(-3,287/T\right) \ \mathrm{m^6 kmol^{-2} s^{-1}}, \tag{6}$$

$$k_{KSAR,KSAR} = 6.35 \times 10^6 \exp\left(-1,590/T\right) \ \mathrm{m^6 kmol^{-2} s^{-1}}, \tag{7}$$

$$k_{KSAR,H_2O} = 3.98 \times 10^8 \exp\left(-3,924/T\right) \ \mathrm{m^6 kmol^{-2} s^{-1}}. \tag{8}$$

In addition to the amino acid reactions above, another reaction was considered for the KSAR model. It is common practice to produce KSAR by the reaction of sarcosine with an aqueous KOH solution. Potassium hydroxide dissociates in water, and a significant concentration of hydroxide ions is left in the solution after sarcosine is added and reacts with the dissociated potassium ions. Carbon dioxide reacts with the remaining hydroxide ions as follows:

$$CO_2(aq) + \mathrm{OH}^- \rightarrow \mathrm{HCO_3}^-. \tag{9}$$

Again, this reaction was considered to be second order and irreversible. The rate coefficient k_{KOH} was calculated as follows [27]:

$$k_{KOH} = k^{\infty}_{KOH} \exp\left(\beta_{CO_2} I\right). \tag{10}$$

Here, I is the ionic strength of the hydroxide in solution in units of kmol/m^3, and k^{∞}_{KOH} is the reaction rate at infinite dilution, given as:

$$k^{\infty}_{KOH} = 3.27869 \times 10^{13} \exp\left(-54,971/RT\right). \tag{11}$$

Where R is the universal gas constant, and the coefficient β_{CO_2} is described by a temperature-dependent relation valid from 20°C to 50°C:

$$\beta_{CO_2} = \left(3.3968 \times 10^{-4}\right) T^2 - \left(2.1215 \times 10^{-1}\right) T + 33.506. \tag{12}$$

These mechanisms, which contain two reactions for MEA solvents and three for KSAR solvents, describe the consumption of CO_2 in the liquid film. The reactions can be combined to calculate an effective rate of consumption for CO_2 for each solvent as follows:

$$r_{CO_2}^{MEA} = -\left(k_{MEA,MEA}[\mathrm{MEA}]^2 + k_{MEA,H_2O}[\mathrm{MEA}][\mathrm{H_2O}]\right)[\mathrm{CO_2}(aq)], \tag{13}$$

$$= -k_{app}^{MEA}[\mathrm{CO_2}(aq)], \tag{14}$$

$$r_{CO_2}^{KSAR} = -\left(k_{KSAR,KSAR}[\mathrm{KSAR}]^2 + k_{KSAR,H_2O}[\mathrm{H_2O}][\mathrm{KSAR}] + k_{KOH}[\mathrm{OH^-}]\right)[\mathrm{CO_2}(aq)], \tag{15}$$

$$= -k_{app}^{KSAR}[\mathrm{CO_2}(aq)]. \tag{16}$$

2.3. Mass Transfer Model

The mass transfer of a species between two phases is in general dependent on conditions on either side of the interface. In this work, we consider only the absorption and reaction of CO_2, and as such all equations below describe the behavior of CO_2 in this system. However, this framework is generalizable to any reacting and absorbing problem if the required physiochemical constants are available. The overall mass transfer rate coefficient K_{CO_2} can be expressed as the harmonic mean of the rate contributions from both the liquid and gas sides of the interface, as shown in Equation (17).

$$K_{CO_2} = \left(\frac{RT}{k_g} + \frac{H_{CO_2}}{E k_l}\right)^{-1} \tag{17}$$

Here, k_g and k_l are the local gas- and liquid-side mass transfer coefficients associated with physical mass transfer phenomena such as diffusion and flow in each phase. The quantity E is an enhancement factor accounting for chemical reactions, and H_{CO_2} is the Henry coefficient for CO_2 in the water–KSAR or water–MEA mixture, depending on the solvent being used, and was computed using the N_2O analogy [28]. The overall interfacial mass transfer rate is then expressed as a function of the rate coefficient; the partial pressure of CO_2 in the gas phase, P_{CO_2}; and the equilibrium partial pressure of $CO_2(aq)$ in the liquid phase, P^*, calculated from Henry's law:

$$N_{CO_2} = K_{CO_2}\left(P_{CO_2} - P^*\right). \tag{18}$$

This rate can be related to the volumetric mass transfer term, $\dot{m}$, using the interfacial area density, a_i, and molecular weight of CO_2, MW_{CO_2}:

$$\dot{m} = a_i MW_{CO_2} N_{CO_2}. \tag{19}$$

In this work, the gas-side coefficient, k_g, was taken from the work of Wang et al. [29], which has been successfully used for packed structures, as

$$k_g = \frac{0.021 D_{CO_2,G}}{d_h}\beta\gamma, \text{ where} \tag{20}$$

$$\beta = \left(\frac{\mu_g}{\rho_g D_{CO_2,G}}\right)^{0.333}, \text{ and} \tag{21}$$

$$\gamma = \left(\frac{\rho_g u_g d_h}{\mu_g(1-\epsilon)}\right)^{0.8}. \tag{22}$$

In Equations (20), (21), and (22), d_h and ϵ represent the hydraulic diameter and the porosity level of the TPMS geometry, respectively. The coefficient for Equation (20) was adjusted to match the experimental results given that the expression was developed for a different type of geometry. There are several classical models for the liquid-side mass transfer coefficient, with the most popular two being the slip-penetration model of Higby [30] and the eddy cell model of Lamont et al. [31]. However, in this work, the liquid-side mass transfer coefficient was eliminated by assuming that the Hatta number, Ha, defined in Equation (23), was approximately equal to the enhancement factor. This assumption was observed to be true through a range of operating parameters during preliminary work by the authors in which the liquid-side mass transfer coefficient was explicitly calculated using the eddy cell model [31]. In this range, it is valid to assume that the enhancement factor, E, is approximately equal to the Hatta number, yielding a simplified expression for the overall mass transfer coefficient as shown in Equation (24).

$$Ha = \frac{\sqrt{D_{CO_2,l} k_{app}}}{k_{l,CO_2}} \tag{23}$$

$$K_{CO_2} = \left(\frac{RT}{k_g} + \frac{H_{CO_2}}{\sqrt{D_{CO_2,l} k_{app}}} \right)^{-1} \tag{24}$$

Here, $D_{CO_2,l}$ represents the diffusivity of CO_2 in the liquid film.

2.4. Case Setup and Meshing Procedure

In this work, the governing equations were solved for a series of cases with varying unit cell size (1, 2, and 4 cm) and porosity (50, 70, and 90%). Each combination of geometric parameters was repeated for two chemical solvents, KSAR and MEA, both in a 30% mass-weighted aqueous solution unless otherwise mentioned. The gas phase is taken to be a mixture of 440 ppm carbon dioxide and the remainder nitrogen. The computational domain for all cases consists of a gyroid TPMS shape measuring 16 cm in the gas flow (x) direction, 8 cm in the film flow (y) direction, and the width of a single unit cell in the third (z) direction. Periodic boundaries were enforced in the third direction to represent the behavior of a much larger system; this choice was observed to deviate minimally from simulations with larger domains in initial testing. As the contactor structure is typically constrained by size, and performance is often measured in volumetric terms (i.e., how much CO_2 can be absorbed from a given volume), the mass flow rate of gas and capture solvent are prescribed to be identical per unit width in all cases; the volumetric gas flow rate per unit width is 1.29×10^{-4} m^3/(s-m), and the solvent flow rate per unit width is 6.31×10^{-2} kg/(s-m). Thus, the total flow rate for the 4 cm unit cell size is four times as large as the flow rate for the 1 cm unit cell size. All results presented below have been adjusted for this factor where appropriate. These conditions and geometries correspond to gas Reynolds numbers of approximately $Re_g = 93$ to 667. The film Reynolds number is defined as $Re_l = \Gamma / 4\mu_l$, where Γ is the mass wetting rate per unit length (kg/(m-s)), with the length here being the actual length of the film inlet, not the unit cell width. This quantity remains essentially constant at $Re_l = 0.07$, with minor variation introduced as the porosity varies.

In all cases, film was introduced from the top edges of the resulting geometry and ran down the TPMS surface, and the gas phase was blown from one side in a cross-flow configuration. The TPMS surface was assumed to be adiabatic, and no-slip conditions were applied there. At the film inlet, liquid thickness and velocity were calculated from the Nusselt solution and applied to keep the wetting rate per unit width constant. As such, these simulations neglect the effects of uneven distribution of solvent at the top of the packing material. Both the gas and the film are introduced at a temperature of 298 K, unless otherwise stated. An outlet condition was prescribed for the film at the bottom edge of the TPMS structure. For the gas phase, a constant flow rate was applied on the left side of the domain, and pressure outlet conditions were applied on the right.

TPMS surface files were generated using the MSLattice program [6], which accepts as inputs the unit cell size, density (ratio of solid wall to airspace in the unit cell), and TPMS type. It also allows for functional grading, in which parameters such as the porosity (fraction of void space within the contactor volume) vary in one or more directions. The computational mesh was constructed by creating a polyhedral background mesh with the same physical dimensions as the TPMS surface and a characteristic cell size of 5% of the unit cell width; then, a Boolean subtract operation was

used to remove the solid region produced by MSLattice from the background mesh, and establish the TPMS walls as boundaries. The film-gas interface was resolved by extruding a small boundary layer containing 4 cells from the TPMS wall with a thickness of 1% of the unit cell width. The first boundary layer cell was stripped from the fluid region and assigned to the film region, where the thickness-averaged finite area equations were solved. At the end of the TPMS geometry opposite from the gas inlet, the surface mesh was extruded normal to the flow direction to yield a more ordered mesh structure, a step that was required to eliminate instabilities arising from flow reversal at the outlet during the simulation start-up. A schematic of the domain and mesh is given in Figure 2.

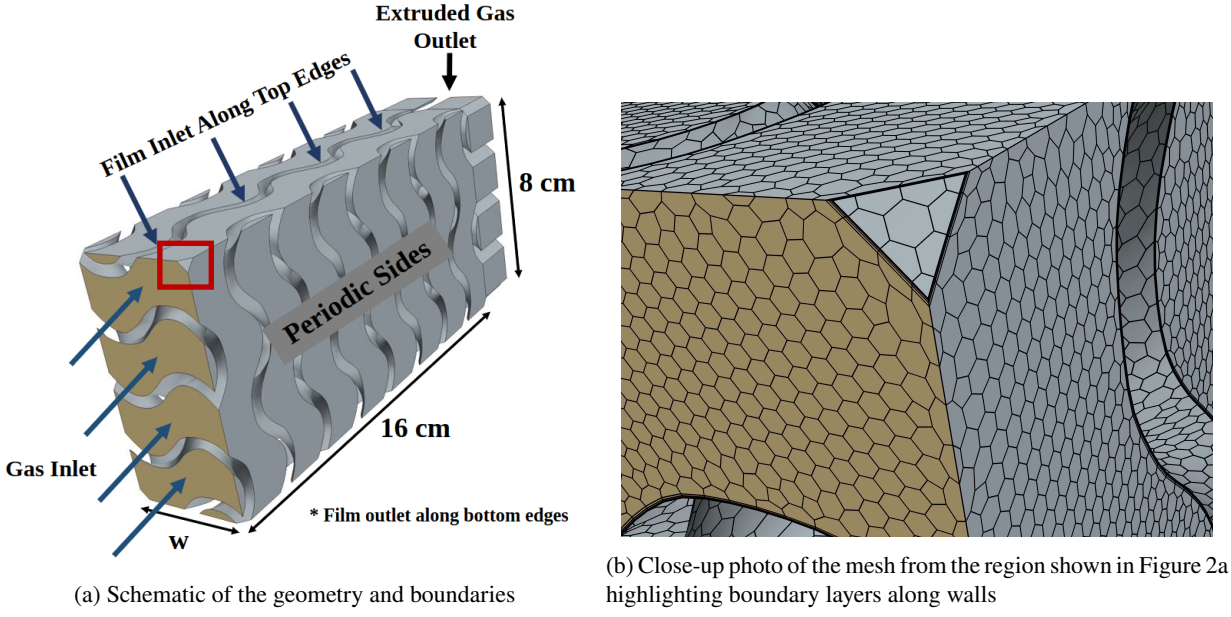

(a) Schematic of the geometry and boundaries

(b) Close-up photo of the mesh from the region shown in Figure 2a highlighting boundary layers along walls

Figure 2: Overview of the solution domain and computational mesh. The 4 cm unit cell case is shown for visual clarity.

Each case was advanced from initially stagnant, uniform conditions using a transient solution algorithm with 20 outer corrector loops. The time step was selected to yield a maximum CFL number of 1.0. Cases were stopped once the outlet concentration of CO_2 reached a quasi-steady state; then, the performance metrics were calculated, and other post-processing activities were completed.

2.5. Validation

Prior to validation against experiments, a grid size sensitivity analysis was conducted to ensure the independence of the solution from the chosen mesh parameters. For this case, we chose a TPMS geometry with a 1 cm unit cell size and 70% porosity, with KSAR as the capture solvent. Three base cell sizes, 10, 5, and 2.5% of the unit cell size, were used to generate a mesh and the capture efficiency and pressure drop were recorded for each case, as shown in Table 2. Between the three tested mesh sizes, the capture efficiency varied less than 1.5% in magnitude, and the pressure drop less than 3.5%. As such, we proceeded with the base mesh size with a characteristic width of 5% of the unit cell size, as the best balance of speed and accuracy.

Next, the numerical approach and mesh setup were validated against the experimental results of An et al. [26]. In their experiments, the authors tested the effects of the gas temperature (35°F, 65°F, and 95°F) and flow rate (1 to 3 L/s through a 10 cm wide by 8 cm tall test section) using a 1 M aqueous KSAR solution as the capture fluid in a unit cell size of 1 cm with 70% porosity. Figure 3 compares the CO_2 capture efficiency, calculated as

$$\eta = 1.0 - \frac{C_{CO_2,out}}{C_{CO_2,in}}, \tag{25}$$

Table 2
Results of grid size independence study for TPMS geometry with 1 cm unit cell size, 70% porosity, and KSAR solvent

	Mesh 1	Mesh 2	Mesh 3
Base cell size (% of unit cell size)	10	5	2.5
Total number of cells	1.7×10^6	6.7×10^6	47×10^6
Capture efficiency (%)	31.79	31.99	32.20
Pressure drop (Pa)	4.053	4.065	4.194

with the experimental results for different gas temperatures. Importantly, An et al. [26] reported different relative humidity levels for the gas stream, but humidity in the gas stream was not modeled in the present simulations. The present computational results show the correct trend of growing efficiency with increasing temperature. Additionally, very good agreement was obtained with experimental data at 35°F and 65°F, well within the experimental error reported by An et al. However, at 95°F, the simulations significantly under-predicted the capture efficiency. Several factors may contribute to this discrepancy, including uncertainty in the experimentally-determined temperature-dependent reaction kinetics and thermophysical properties, and the omission of water vapor and associated interactions from the numerical model. However, the present work did not rely on the model's temperature dependence to reach any conclusions and therefore is deemed appropriate. Section 2.2 shows that a high temperature and high concentration of H_2O in the film enhance k_{app}, which increases K_{CO_2} and consequently the capture of CO_2 by the liquid film. Thus, at high temperatures, not accounting for the absorption of water vapor by the liquid film has a larger impact.

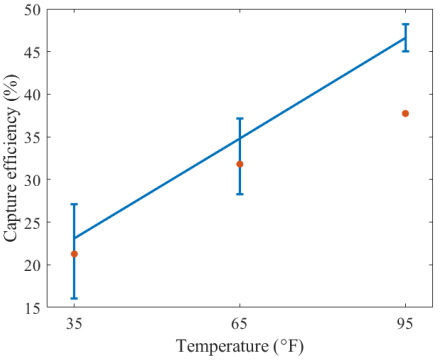

Figure 3: Comparison between the experimental results of An et al. [26] (error bar) and the computational results (red dots).

In addition to varying the ambient temperature, the effects of increasing the gas flow rate were compared with the experimental results. When increasing the gas flow rate from 1 to 2 L/s, the model predicted a 14.2% reduction in capture efficiency, compared to the 13% repoted by An et al. [26]. Based on this comparison, we deemed the simulation methodology and mesh setup to be appropriate for the purposes of this study.

3. Results

This section examines the carbon capture performance of TPMS geometries with varying unit cell size and porosity and with KSAR and MEA liquid solvents. Overall performance metrics, such as capture efficiency and gas pressure drop, were extracted for each geometry. Field variables that contributed to the mass transfer behavior were independently analyzed to determine how changes in the geometry and chemistry of the system affected CO_2 absorption. Additionally, the performance of two functionally graded contactors, where the density either increased or decreased in the gas flow direction, was examined.

3.1. KSAR Solvent

The efficiency and pressure drop for each combination of unit cell size and contactor porosity are summarized for the KSAR solvent in Figure 4. Several general trends were observed. The capture efficiency was sensitive to both unit cell size and porosity; however, the sensitivity to unit cell size was weaker at low porosity values. The pressure drop was highly dependent on both unit cell size and porosity. Lower values of both corresponded to more constricted flow passages. The capture efficiency response to changes in both porosity and unit cell size was monotonic. The contours indicate there were no interaction effects between the two metrics. Across the range of input parameters chosen, the smaller the unit cell size and the higher the porosity, the higher the capture efficiency.

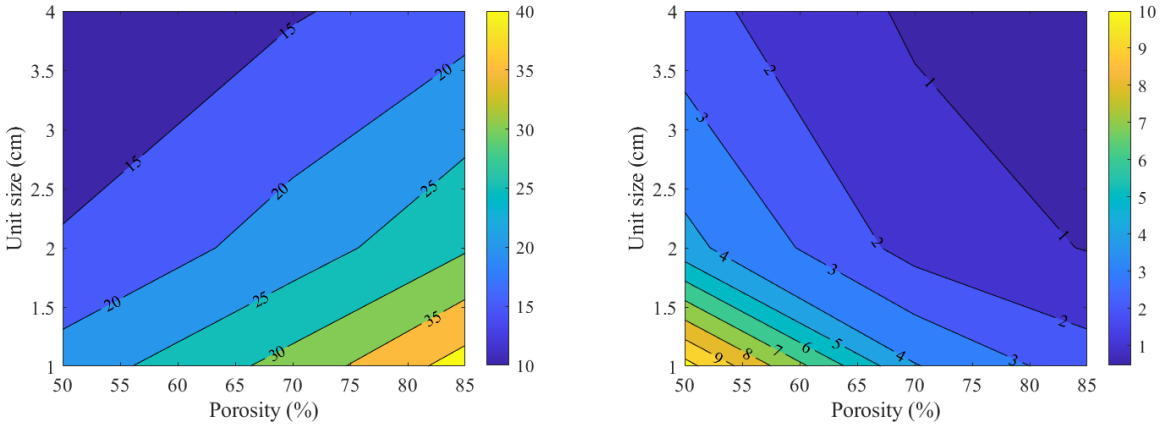

(a) Capture efficiency (%)

(b) Pressure drop (Pa)

Figure 4: Contour plots of contactor performance metrics with varying density and unit cell size for KSAR.

We explain these trends by examining Equation (19), which specifies that the mass transfer rate is dependent on two main quantities: the interfacial area density, a_i, and the interfacial mass transfer rate, N_{CO_2}. The contour plots for the volume-integrated mass transfer, $\dot{m}$, along with the individual contributions of the interfacial surface area, a_i, and volume-integrated interfacial mass transfer rate, N_{CO_2}, are given in Figure 5. Note that volume-integrated quantities have been weighted by the unit cell size to enable comparison between domains of differing physical sizes. The volumetric mass transfer term (Equation [19]) displayed in Figure 5a shows behavior identical to that of the efficiency curves (as expected). It also reveals that the most efficient case absorbed CO_2 from the gas at a rate an order of magnitude faster than that of the least efficient case, per unit volume. Figure 5b illustrates the change in specific surface area (surface area per unit volume, m^2/m^3) with varying TPMS unit cell size and porosity. Over the tested range of parameters, the specific surface area varied by approximately a factor of four, from 150 to 600 m^2/m^3. This quantity was mostly dependent on the unit cell size, as expected; decreasing the unit cell size increased the number of cells (and associated walls) that could be contained in a given volume. This effect explains the increase in both capture efficiency and pressure drop with decreasing unit cell size because the additional surface area offered both more opportunity for mass transfer and more resistance to fluid flow through the TPMS geometry. Figure 5c shows that the interfacial mass transfer rate increased with increasing porosity and unit cell size, contributing to the higher efficiencies observed at large porosity values. However, the magnitude of the increase in interfacial mass transfer at large unit cell sizes was smaller than the decrease in interfacial mass transfer area, leading to overall lower performance with large unit cell sizes. Thus, Figure 5 illustrates that the performance of the TPMS contactor was most dependent on the geometric parameters rather than the mass transfer behavior. Still, variation in mass transfer across the range of geometric parameters was significant. Contributions to these changes are discussed in the following section.

3.1.1. Contributions to Interfacial Mass Transfer

Variations in the interfacial mass transfer rate N_{CO_2} are introduced by several quantities, as discussed in Section 2.3. The difference between the local partial pressure of CO_2 in the gas phase, and the local equilibrium partial pressure calculated from the concentration in the film, is one driving factor. The partial pressure of CO_2 in the gas stream

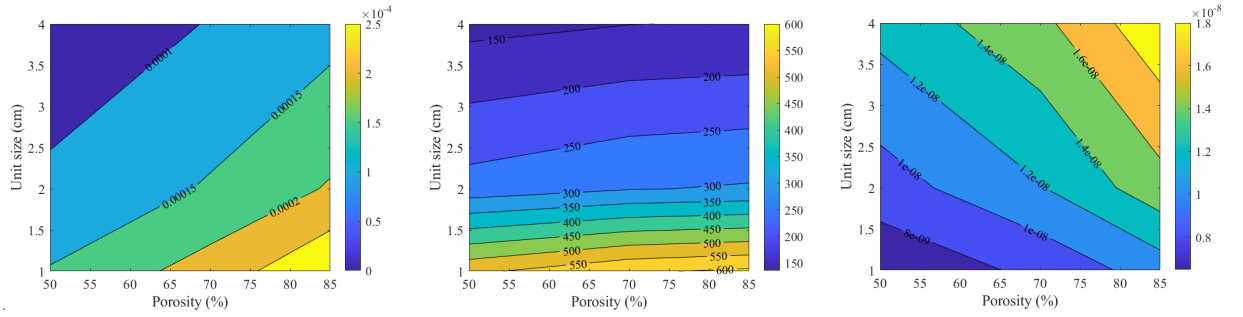

(a) $\dot{m}$ (kg/(m^3-s)) (b) TPMS specific surface area (m^2/m^3) (c) Interface-averaged N_{CO_2} (kmol/(m^2-s))

Figure 5: Contour plots of $\dot{m}$ (Equation [19]), TMPS specific surface area, and interface-averaged N_{CO_2} generated from the results of the parametric sweep for KSAR.

(see Figure 6b) is orders of magnitude larger than the equilibrium partial pressure (see Figure 13 in the Supporting Information) due to the fast reaction kinetics in comparison with the rate of mass transfer, and as such dominates the difference term in Equation 18. However, as shown in Figure 6a, the overall mass transfer rate coefficient varies more substantially across the range of geometric parameters, and thus exerts a larger influence on the interfacial mass transfer rate, which trends closely with the rate coefficient. Both are observed to have the highest values in configurations with large unit cell size and high porosity, in contrast with the partial pressure of CO_2 in the gas phase, which is largest in lower porosity configurations where lower specific surface area and capture efficiency result in higher concentrations of CO_2 in the gas stream.

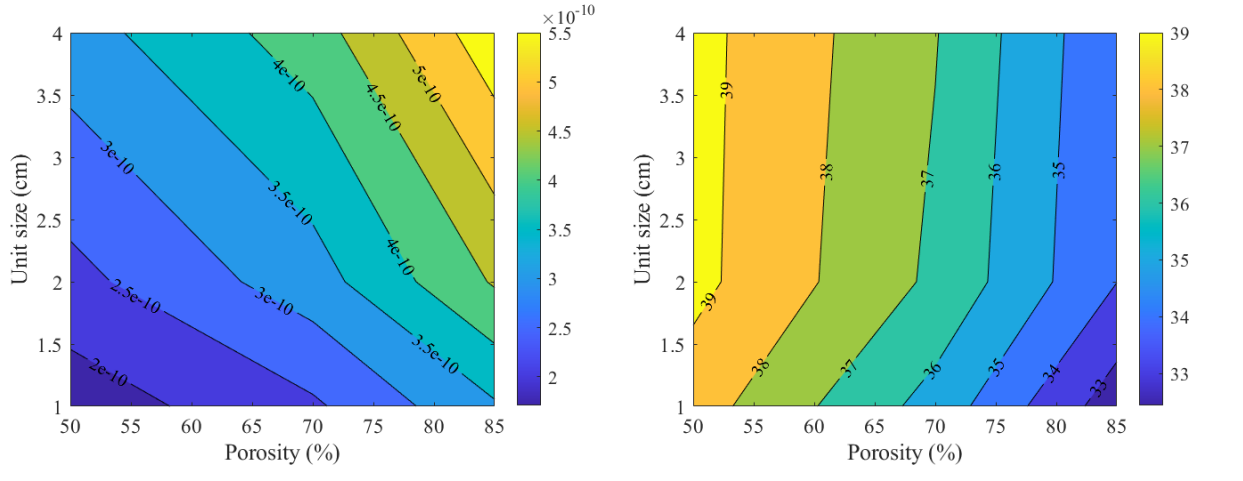

(a) Interface-averaged K_{CO_2} (kmol s/m/kg) (b) Interface-averaged P_{CO_2} (Pa)

Figure 6: Contour plots of interface-averaged K_{CO_2} and P_{CO_2} for KSAR.

According to Equation 24, the overall mass transfer rate coefficient K_{CO_2} is dependent on the gas-side mass transfer rate coefficient, temperature, apparent reaction rate, and thermophysical properties of the solvent. Due to the low concentration of carbon dioxide in DAC applications, and low associated chemical heat generation, the temperature within the system as well as dependent quantities like reaction rate and temperature-dependent properties are essentially constant at all operational conditions tested herein (see Figure 14 in the Supporting Information), even with an adiabatic boundary condition prescribed on the TPMS structure wall. Thus, variations in the overall mass transfer rate should correspond to changes in the gas-side mass transfer coefficient, a trend which is confirmed by Figure 7a. Changes in the gas-side mass transfer rate coefficient are caused by variation of the parameter γ (see Equation 22), which increases

with hydraulic diameter and porosity, leading to the maximum mass transfer rate at the largest unit cell size and porosity value. Some variation in the near-wall gas velocity was observed due to changes in TPMS geometry, but this effect was largely suppressed by the presence of the wall and associated no-slip condition.

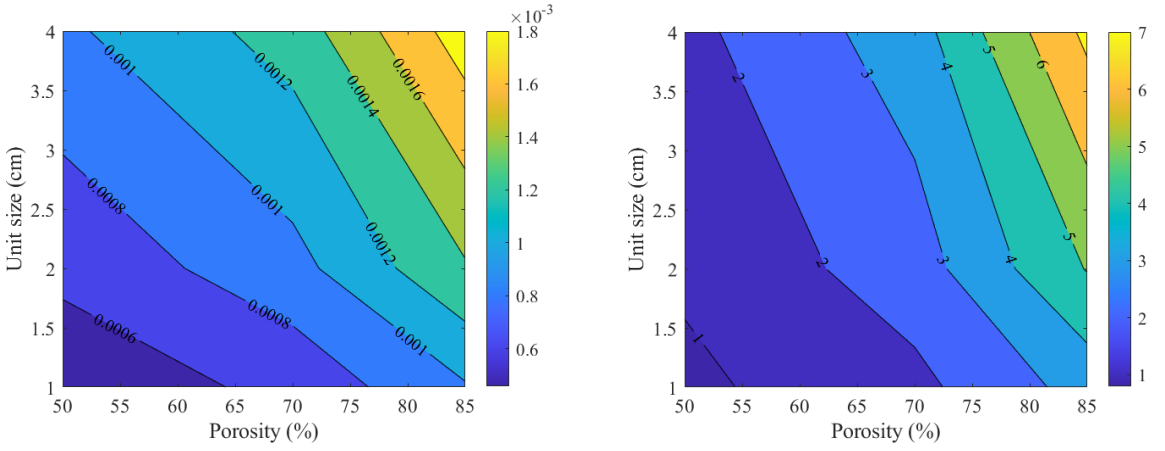

(a) Interface-averaged gas-side mass transfer coefficient, k_g (m/s)

(b) Interface-averaged quantity γ

Figure 7: Contour plots of interface-averaged k_g and γ for KSAR.

Renderings of the main flow variables, including velocity and temperature, are provided in the Supporting Information. While these variables did not significantly impact variations the mass transfer behavior of the system, they have been included to enable the reader to more effectively visualize flow through the complex TPMS geometry.

3.2. MEA Solvent

The parametric study of TPMS geometric parameters described above for the KSAR solvent was repeated with a MEA solvent to quantify the effect of the solvent choice on the capture efficiency of the system. Although the pressure drop performance is identical to the KSAR solvent, the MEA solvent offered slightly higher capture efficiency, with a maximum value of 43% in the tested cases, as shown in Figure 8a. As the specific surface area for corresponding KSAR and MEA cases is identical, changes in the interfacial mass transfer rate must explain the observed differences in performance.

Comparison of Figure 8b with Figure 6a confirms that the overall mass transfer rate coefficient is larger for the MEA solvent, and as shown by Figure 8c, changes in the gas-side mass transfer rate coefficient again drive variations in the overall mass transfer behavior. However, differences between the KSAR and MEA solvent performance arise as a result of differing physical and chemical properties between the two solvents, notably the volatility of CO_2 in the solvent (inverse Henry's constant, denoted herein as H_{CO_2}) which is directly involved in the calculation of the overall mass transfer rate coefficient. The MEA solvent had an volatility value approximately 70% lower than the KSAR solvent, contributing to a higher overall mass transfer rate. Additionally, the diffusivity of CO_2 in MEA is roughly 26% larger than in KSAR, contributing to an increased gas-side mass transfer rate coefficient. Although the apparent reaction rate observed for the KSAR solvent was almost twice as large as for MEA (approximately 7.3×10^{-4} s^{-1} for KSAR and 4.0×10^{-4} s^{-1} for MEA, as shown in the Supporting Information), the dependence of the overall mass transfer rate coefficient on the apparent reaction rate is of order 0.5, and thus is dominated by a reduced gas-side mass transfer coefficient and absorptivity when compared to the MEA solvent.

3.3. Functionally Graded Contactor

Naturally, the conditions within the TPMS contactors described above are highly nonuniform, with the driving factors of mass transfer at their maximum values as the gas is introduced at the inlet and tapering sharply as the gas moves toward the outlet. This is because the concentrations of both CO_2 in the gas and solvent in the liquid film are highest

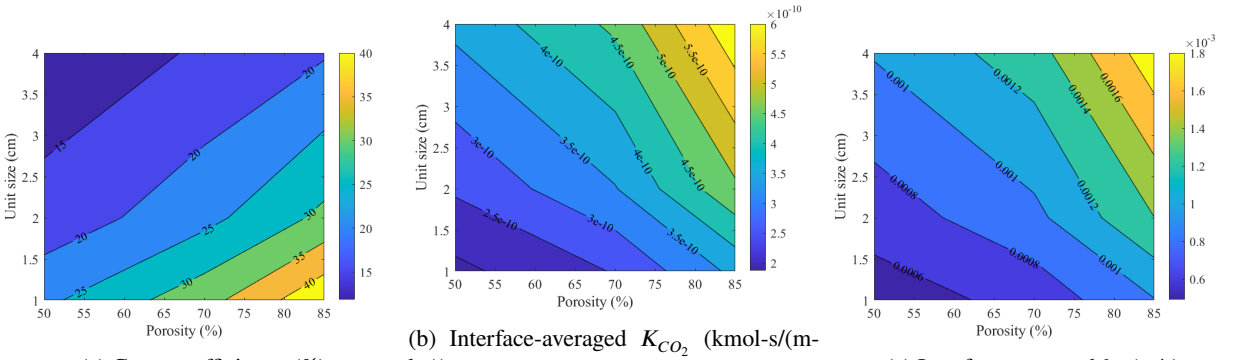

(a) Capture efficiency (%)

(b) Interface-averaged K_{CO_2} (kmol-s/(m-kg))

(c) Interface-averaged k_g (m/s)

Figure 8: Contour plots of capture efficiency, overall mass transfer rate coefficient, and gas-side mass transfer rate coefficient for MEA.

Table 3
Capture efficiency, pressure drop, and a_i of 1 cm cell size graded contactors using MEA.

Porosity (%)	85–50	50–85	50	70	85	Average
Capture efficiency (%)	31.67	32.04	23.92	33.11	44.02	33.68
Pressure drop (Pa)	5.0	5.1	10.4	4.1	2.5	6.5
Specific surface area (m^2/m^3)	580.5	581.2	538.2	593.1	609.7	574

Table 4
Gas-side mass transfer coefficient and gas velocity for the 1 cm cell size graded contactors using MEA.

Porosity (%)	85–50	50–85	50	70	85	Average
k_g (m/s)	6.47×10^{-4}	6.53×10^{-4}	4.91×10^{-4}	6.7×10^{-4}	9.91×10^{-4}	7.17×10^{-4}
u_g (m/s)	9.92×10^{-3}	1.00×10^{-2}	9.80×10^{-3}	1.03×10^{-2}	1.02×10^{-2}	1.00×10^{-2}

as each fluid is introduced into the domain and taper as CO_2 is absorbed by and reacts with the solvent. The spatial variation of these quantities could be accounted for in an intelligent contactor design by varying the parameters of the TPMS to tailor the local geometry to the expected conditions at each location. This would result in a functionally graded contactor where the porosity level gradually changes within the unit cell, as shown in Figure 9. Here, for exploratory purposes, only a 1 cm unit cell size and MEA as a solvent were considered with two gradually changing porosity levels: in one case, the porosity began at 85% near the gas inlet and dropped to 50% at the gas outlet (the 85%–50% setup); in the second, this gradient was reversed so that the porosity was lowest at the gas inlet (the 50%–85% setup). Table 3 presents the efficiencies, pressure drops, and specific surface areas for these two new setups and the results obtained for the constant-porosity cases. The average values of the constant-porosity cases are given in the last column. Among the functionally graded cases, the results can be considered identical. In addition, no clear advantage is observable when comparing the functionally graded cases with the constant-porosity cases. A quick analysis shows that both scenarios had efficiencies slightly smaller than the average of the 50% and 85% porosity level cases and smaller pressure drops. Interestingly, the functionally graded contactors had higher specific surface areas than the average, but that did not improve efficiency. The reason for this is the lower gas-side mass transfer coefficient, as given in Table 4, which was caused by smaller interfacial averaged gas velocities. Note that the gas-side mass transfer coefficient is calculated based on the average porosity, and thus there is only one value for the whole contactor. Additionally, to enable predictions of functionally graded surfaces, the gas-side mass transfer model used here likely needs to be modified, and a less empirical model likely needs to be used. This needs to be explored further in future work. Based on the present results, the examined functionally graded surfaces yielded worse performance and pressure drops than a case with a single high porosity level. Another alternative that can be explored in the future is the use of multimorphology lattices such as a hybrid between the gyroid and Fischer–Koch surfaces (or other types of TPMS surfaces) to maximize the capture efficiency by maximizing the specific surface area and the gas velocity inside the unit cell.

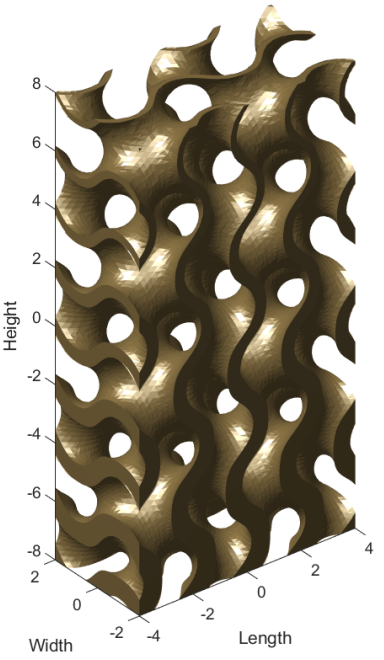

Figure 9: Visualization of gyroid TPMS structure with porosity parameter graded in vertical direction (generated with MSLattice [6])

4. Discussion

As discussed in Section 3.1, the specific interfacial surface area dominates the efficiency and pressure drop metrics for the TPMS contactor geometries, at least for the test conditions chosen for this work. However, a significant variation in the interfacial mass transfer rate occurs that, if well understood, could be tuned to further increase the contactor performance. In addition, differences in performance were observed between the KSAR and MEA solvents; the MEA solvent achieved a maximum efficiency of 49%, but the KSAR solvent was able to capture only 42% of the CO_2 under the same conditions. This change is largely attributable to the differences in the physiochemical properties of the solvents; for instance, the Henry's coefficients of CO_2 were 2.27×10^6 Pa-m^3/kmol in the MEA solution and approximately 3.85×10^6 Pa-m^3/kmol in the KSAR solution. This should have increased absorption rates into the MEA solvent in regions where the liquid-side mass transfer considerations were dominant, in accordance with Equation (24).

Other properties also influenced the absorption of CO_2 into the solvent. The diffusivity of CO_2 in the MEA solvent was approximately 74% of the value for KSAR. Additionally, comparing Figures 14b and 15 shows that the apparent reaction rate of CO_2 in MEA was roughly 55% of that in KSAR in all tested cases. Both of these properties should have caused KSAR to perform better than MEA; however, because they are incorporated into a square root term in Equation (24), their benefits were offset by the higher solubility of CO_2 in MEA than in KSAR, which appears as a linear term in the calculation of the interfacial mass transfer rate. From this analysis and the discussion in Section 3.1, it can be safely concluded that the specific surface area of the contactor and solubility of CO_2 in the liquid film were the two dominant factors that influenced performance in the cases presented herein.

The functionally graded geometries presented in Section 3.3 were originally proposed to determine whether changes in the specific surface area and cross-sectional area over the length of the contactor could be used to improve absorption efficiency. Because of limitations of the gyroid generation software MSLattice, only basic changes were able to be tested. The porosity of the TPMS was varied from 50% to 85%, and inversely from 85% to 50%. Higher porosity near the outlet of the contactor was hypothesized to lead to slower gas flow and more contact time, whereas lower porosity at the beginning was hypothesized to offer more interfacial surface area for mass transfer to occur. Grading the geometry also reduced the length of the low-porosity contactor, where the most pressure drop is likely to occur. As

shown in Table 3, the functionally graded contactors did exhibit a 23% lower pressure drop than the average value for the uniform-porosity geometries, which would reduce pumping losses in a physical installation. However, the efficiency of both graded configurations was also 5% lower than the average of the uniform geometries. A more holistic system-level analysis with an improved model for the gas-side mass transfer coefficient would be required to determine whether the trade-off of lower pressure drop for slightly lower efficiency and increased manufacturing complexity is worthwhile.

Finally, the results presented herein are highly sensitive to the models chosen for the mass transfer and chemical processes that occur in carbon capture. Thermophysical and chemical data are difficult to measure experimentally, particularly for reacting systems such as CO_2 and amino acid solvents. Therefore, there is significant uncertainty in many of the parameters used in this work. However, every effort was made to use reliable data when available and to include the effects of temperature and other environmental changes. A complete list of thermophysical and chemical properties and relationships used in this work with sources is available in Appendix A.

5. Conclusion

In this work, a computationally efficient thin-film CFD model was used to interrogate the performance of gyroid TPMS structures for DAC applications. The numerical model included a comprehensive description of physical and chemical processes which contribute to the absorption and reaction of CO_2 into amine solvents, and was validated against published experimental data. The model was then used to compute the efficiency and pressure drop of structures with varying TPMS parameters, such as porosity and unit cell size. Individual effects of key physical and chemical processes were isolated and their overall contribution to system efficiency was quantified. Through this process, several key conclusions were drawn, including:

- The overall performance of the TPMS contactor geometry is determined largely by the specific surface area of the contactor itself, rather than by changes in the flow or mass transfer behavior introduced by variations in contactor geometry.
- While not a significant factor in overall performance, some variation in the interfacial mass transfer rate was observed between cases, largely as a result of changes the gas-side mass transfer rate coefficient. The apparent reaction rate did not significantly affect performance of cases with the same solvent, as all cases were nearly isothermal owing to the low CO_2 loading which limited the heat generated by chemical reactions.
- The MEA solvent performed slightly better in all conditions than the KSAR solvent. Differences between the KSAR and MEA solvents are largely attributable to changes in physiochemical properties such as the absorptivity and diffusivity of CO_2 in the solvents, rather than differences in the chemical kinetics of the system.
- Attempts to use simple functional grading techniques to tailor the local TPMS geometry to the expected conditions did not produce significant differences in system efficiency, although it did decrease pressure drop when compared to the average of uniform TPMS structures. Significant system-level optimization will be required to fully leverage functionally graded structures for DAC and other applications.

Future work will expand this simple parametric study to include the changes of other operational parameters including gas velocity, gas/liquid loading ratio, and other metrics which could be used to optimize the performance of a given system. The relative simplicity of the thin-film model will also allow simulations to be scaled to the device level with relative ease, allowing for prediction of effects such as solvent stripping or uneven distribution to be captured. This work will contribute to the optimization of DAC contactor systems and assist in the reduction of overall system cost, potentially leading to more widespread industrial adoption.

6. Acknowledgments

This work was sponsored by the US Department of Energy's Building Technologies Office under Contract No. DE-AC05-00OR22725 with UT-Battelle, LLC.

A. Thermophysical Constants

The thermophysical constants used to determine the transport and chemical phenomena of this problem are given in the following tables.

Table A.1: Transport properties

Symbol	Value	Unit	Source
ρ_l	1,010	kg/m^3	[9]
μ_l	2.41×10^{-3}	Pa-s	[9]

Table A.2: Mass transfer properties

Symbol	Value	Unit	Source
$D_{CO_2,KSAR}$	$4.406 \times 10^{-11}T - 1.16337 \times 10^{-8}$	m^2/s	[27]
$H_{CO_2,KSAR}$	$1.091 \times 10^{5}T - 2.79579 \times 10^{7}$	Pa-m^3/kmol	[27]
$D_{CO_2,MEA}$	1.66×10^{-9}	m^2/s	[28]
$H_{N_2O,MEA}$	2.85×10^{6}	Pa-m^3/kmol	[32]
H_{N_2O,H_2O}	3.69×10^{6}	Pa-m^3/kmol	[33]
H_{CO_2,H_2O}	2.94×10^{6}	Pa-m^3/kmol	[34]

B. Supporting Information

B.1. Flow Visualizations

This section contains visualizations of the velocity and temperature distributions within the TPMS structure which, although not significant contributors to the variation in overall mass transfer, are unique to TPMS structures. Figure 10 shows the flow streamlines for the extreme values of unit cell size and porosity presented in this study. In all cases, the flow closely follows the TPMS surface with no evidence of separation or recirculation, owing to the low Reynolds numbers of each case. The maximum velocity magnitude varies slightly due to differences in overall flow area as the porosity changes, but insignificantly compared to the dominant factors in the mass transfer behavior, such as specific surface area of the structure.

Figure 11 shows a cross section of the gas phase velocity field for a range of TPMS geometric parameters. The flow pattern appears to develop after passing through a few unit cells in the flow direction, leading to homogeneous conditions between cells for the 1 cm unit cell size case. For the larger unit cell size, the relatively low number of unit cells contained in the test section results in some differences between cells.

Figure 12 shows the temperature profile within the gas flow for a range of TPMS parameters. As expected due to the low CO_2 loading, the heat of reaction is not significant enough to cause notably elevated temperatures, even with an adiabatic condition imposed on the TPMS wall (i.e., no cooling mechanism). A small increase in temperature is observed near the bottom corner of the contactor near the gas inlet; this is expected as the film has had the longest time to react at this location, and the CO_2 concentration is highested near the gas inlet. In higher load conditions, the heat of reaction may contribute to elevated temperatures within the system, necessitating the incorporation of temperature-dependent thermophysical properties and reaction kinetics to achieve accurate results.

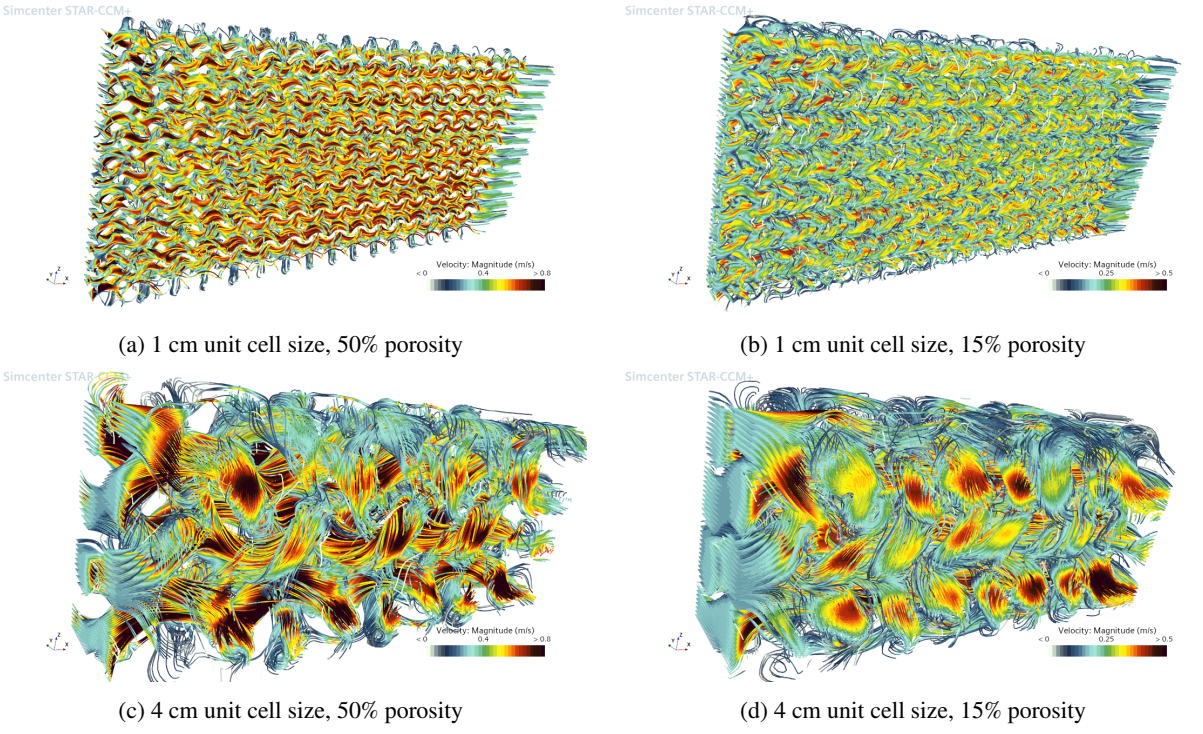

(a) 1 cm unit cell size, 50% porosity

(b) 1 cm unit cell size, 15% porosity

(c) 4 cm unit cell size, 50% porosity

(d) 4 cm unit cell size, 15% porosity

Figure 10: Gas velocity streamlines shown for several of the tested TPMS geometric configurations

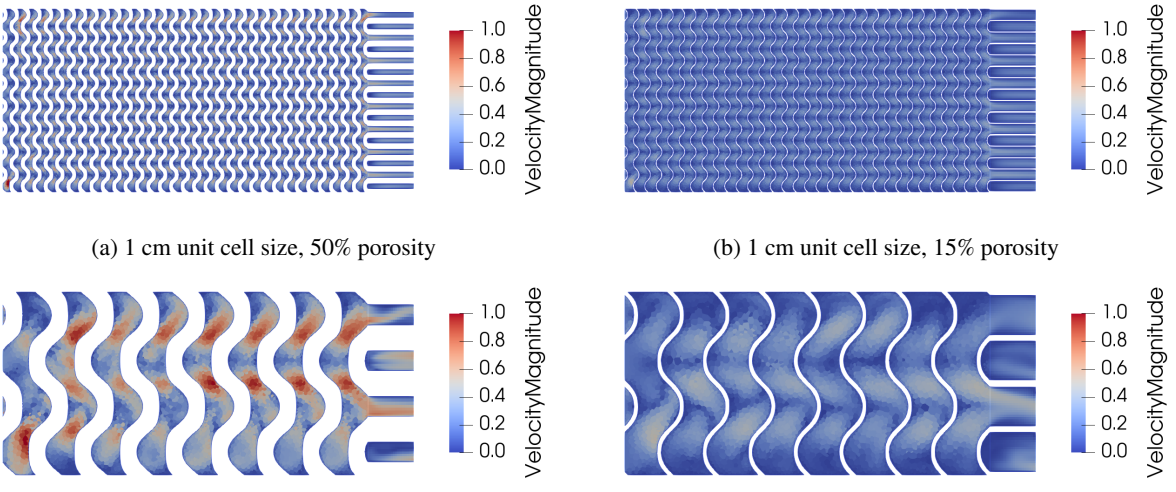

(a) 1 cm unit cell size, 50% porosity

(b) 1 cm unit cell size, 15% porosity

(c) 4 cm unit cell size, 50% porosity

(d) 4 cm unit cell size, 15% porosity

Figure 11: Cross sections of the gas velocity field within the interior of the TPMS structure. The gas phase flows from left to right; the liquid phase (not shown) flows from top to bottom.

B.2. Mass Transfer Variables

This section contains results of quantities which were not observed to vary significantly across the tested range of geometric and operational parameters, and as such do not contribute significantly to the discussion on the effect on mass transfer. They have been included here for completeness.

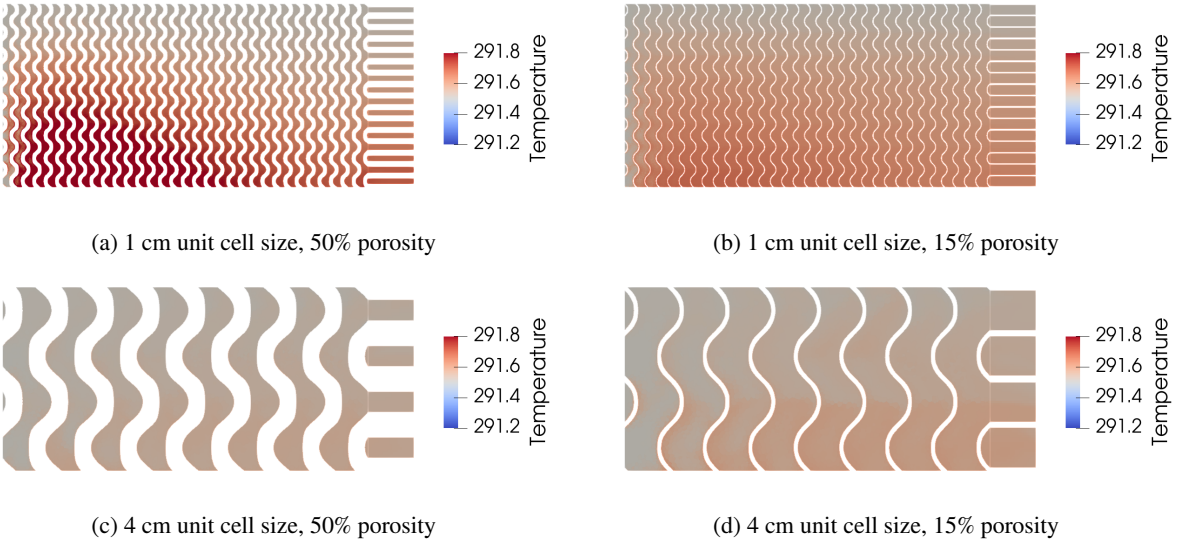

(a) 1 cm unit cell size, 50% porosity

(b) 1 cm unit cell size, 15% porosity

(c) 4 cm unit cell size, 50% porosity

(d) 4 cm unit cell size, 15% porosity

Figure 12: Cross sections of the gasmtemperature field within the interior of the TPMS structure

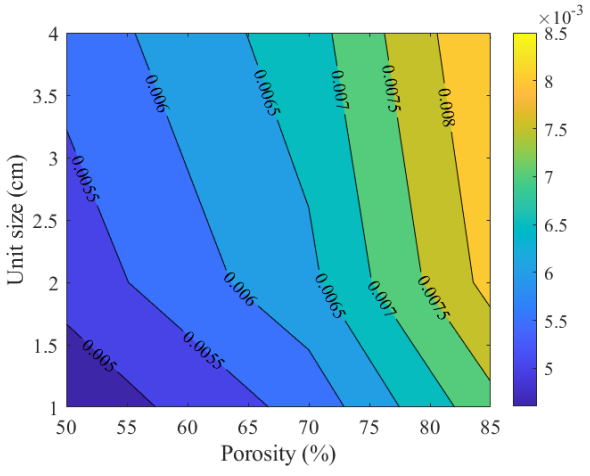

Figure 13: Interface-averaged equilibrium partial pressure, P^*, for KSAR solvent in different contactor geometries

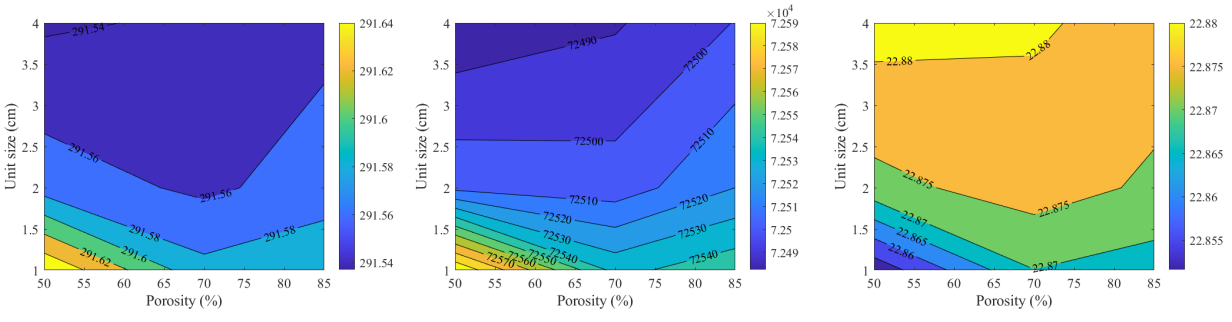

(a) Interface-averaged T (K)

(b) Interface-averaged k_{app} (s^{-1})

(c) Interface-averaged β

Figure 14: Contour plots of interface-averaged T, k_{app}, and β for KSAR solvent in different contactor geometries

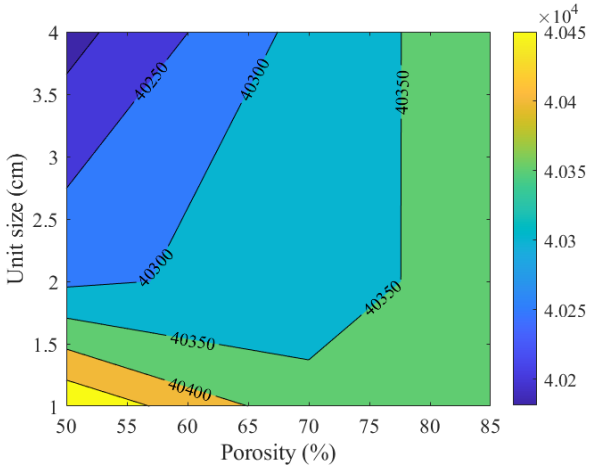

Figure 15: Interface-averaged k_{app} (s^{-1}) for MEA solvent in different contactor geometries

References

[1] J. Iyer, T. Moore, D. Nguyen, P. Roy, and J. Stolaroff. Heat transfer and pressure drop characteristics of heat exchangers based on triply periodic minimal and periodic nodal surfaces. *Applied Thermal Engineering*, 209, 6 2022. ISSN 13594311. doi: 10.1016/j.applthermaleng.2022.118192.

[2] B.W. Reynolds, C.J. Fee, K.R. Morison, and D.J. Holland. Characterisation of heat transfer within 3D printed tpms heat exchangers. *International Journal of Heat and Mass Transfer*, 212, 9 2023. ISSN 00179310. doi: 10.1016/j.ijheatmasstransfer.2023.124264.

[3] D.W. Abueidda, M. Elhebeary, C.S.A Shiang, S. Pang, R.K. Abu Al-Rub, and I.M. Jasiuk. Mechanical properties of 3D printed polymeric gyroid cellular structures: Experimental and finite element study. *Materials and Design*, 165, 3 2019. ISSN 18734197. doi: 10.1016/j.matdes.2019.107597.

[4] L. Wallat, P. Altschuh, M. Reder, B. Nestler, and F. Poehler. Computational design and characterisation of gyroid structures with different gradient functions for porosity adjustment. *Materials*, 15, 5 2022. ISSN 19961944. doi: 10.3390/ma15103730.

[5] O. Al-Ketan, D. W. Lee, R. Rowshan, and R. K. A Al-Rub. Functionally graded and multi-morphology sheet TPMS lattices: Design, manufacturing, and mechanical properties. *Journal of the mechanical behavior of biomedical materials*, 102:103520, 2020.

[6] O. Al-Ketan and R.K. Abu Al-Rub. MSLattice: A free software for generating uniform and graded lattices based on triply periodic minimal surfaces. *Material Design and Processing Communications*, 3, 12 2021. ISSN 25776576. doi: 10.1002/mdp2.205.

[7] D.W. Keith, G. Holmes, D.S. Angelo, and K. Heidel. A process for capturing CO_2 from the atmosphere. *Joule*, 2(8):1573–1594, 2018.

[8] N.C. Ellebracht, P. Roy, T. Moore, A.E. Gongora, D.I. Oyarzun, J.K. Stolaroff, and D.T. Nguyen. 3D printed triply periodic minimal surfaces as advanced structured packings for solvent-based CO_2 capture. *Energy Environmental Science*, 16(4):1752–1762, 2023.

[9] K.K. Pant and V.K. Srivastava. Carbon dioxide absorption into monoethanolamine in a continuous film contactor. *Chemical Engineering Journal*, 133:229–237, 9 2007. ISSN 13858947. doi: 10.1016/j.cej.2007.02.001.

[10] P. Sobieszuk and R. Pohorecki. Gas-side mass transfer coefficients in a falling film microreactor. *Chemical Engineering and Processing: Process Intensification*, 49:820–824, 8 2010. ISSN 02552701. doi: 10.1016/j.cep.2010.06.010.

[11] T. Sema, A. Naami, K. Fu, M. Edali, H. Liu, H. Shi, Z. Liang, R. Idem, and P. Tontiwachwuthikul. Comprehensive mass transfer and reaction kinetics studies of CO_2 absorption into aqueous solutions of blended MDEA-MEA. *Chemical Engineering Journal*, 209:501–512, 10 2012. ISSN 13858947. doi: 10.1016/j.cej.2012.08.016.

[12] D. Asendrych, Niegodajew. P., and S. Drobniak. CFD modelling of CO_2 capture in a packed bed by chemical absorption. *Chemical and Process Engineering - Inzynieria Chemiczna i Procesowa*, 34:269–282, 6 2013. ISSN 02086425. doi: 10.2478/cpe-2013-0022.

[13] Y. Ma, H. Wang, F. Hong, J. Yang, Z. Chen, H. Cui, and J. Feng. Modeling and optimization of combined heat and power with power-to-gas and carbon capture system in integrated energy system. *Energy*, 236:121392, 2021. ISSN 0360-5442. doi: 10.1016/j.energy.2021.121392. URL `https://www.sciencedirect.com/science/article/pii/S0360544221016406`.

[14] J.A. Thompson and C. Tsouris. Rate-based absorption modeling for postcombustion CO_2 capture with additively manufactured structured packing. *Industrial and Engineering Chemistry Research*, 60:14845–14855, 10 2021. ISSN 15205045. doi: 10.1021/acs.iecr.1c02756.

[15] H. Jiang, S. Wang, L. Xing, V.J. Pinfield, and J. Xuan. Machine learning based techno-economic process optimisation for CO_2 capture via enhanced weathering. *Energy and AI*, 12, 4 2023. ISSN 26665468. doi: 10.1016/j.egyai.2023.100234.

[16] A. Sinha, H. Thakkar, F. Rezaei, Y. Kawajiri, and M.J. Realff. Direct air capture of CO_2 in enclosed environments: Design under uncertainty and techno-economic analysis. *Computer Aided Chemical Engineering*, 2018.

[17] T.M. Alabi, N.P. Lawrence, L. Lu, Z. Yang, and R.B. Gopaluni. Automated deep reinforcement learning for real-time scheduling strategy of multi-energy system integrated with post-carbon and direct-air carbon captured system. *Applied Energy*, 333, 3 2023. ISSN 03062619. doi: 10.1016/j.apenergy.2022.120633.

[18] W.L. Li, H.W. Liang, J.H. Wang, L. Shao, G.W. Chu, and Y. Xiang. CFD modeling on the chemical absorption of CO_2 in a microporous tube-in-tube microchannel reactor. *Fuel*, 327, 11 2022. ISSN 00162361. doi: 10.1016/j.fuel.2022.125064.

[19] W.L. Li, J.H. Wang, Y.C. Lu, L. Shao, G.W. Chu, and Y. Xiang. CFD analysis of CO_2 absorption in a microporous tube-in-tube microchannel reactor with a novel gas-liquid mass transfer model. *International Journal of Heat and Mass Transfer*, 150, 4 2020. ISSN 00179310. doi: 10.1016/j.ijheatmasstransfer.2020.119389.

[20] D. Sebastia-Saez, S. Gu, P. Ranganathan, and K. Papadikis. 3D modeling of hydrodynamics and physical mass transfer characteristics of liquid film flows in structured packing elements. *International Journal of Greenhouse Gas Control*, 19:492–502, 2013. ISSN 17505836. doi: 10.1016/j.ijggc.2013.10.013.

[21] D. Sebastia-Saez, S. Gu, P. Ranganathan, and K. Papadikis. Micro-scale CFD study about the influence of operative parameters on physical mass transfer within structured packing elements. *International Journal of Greenhouse Gas Control*, 28:180–188, 2014. ISSN 17505836. doi: 10.1016/j.ijggc.2014.06.029.

[22] D. Sebastia-Saez, S. Gu, P. Ranganathan, and K. Papadikis. Micro-scale CFD modeling of reactive mass transfer in falling liquid films within structured packing materials. *International Journal of Greenhouse Gas Control*, 33:40–50, 2 2015. ISSN 17505836. doi: 10.1016/j.ijggc.2014.11.019.

[23] C.W. Hirt and B.D. Nichols. Volume of fluid (VOF) method for the dynamics of free boundaries. *Journal of Computational Physics*, 39:201–225, 1 1981. ISSN 10902716. doi: 10.1016/0021-9991(81)90145-5. URL `https://linkinghub.elsevier.com/retrieve/pii/0021999181901455`.

[24] F.D.F. Chuahy, K. Kincaid, and K. Nawaz. A thin-film modeling approach for analysis of carbon capture sorbent-based devices. *Carbon Capture Science Technology*, 9:100134, 12 2023. ISSN 27726568. doi: 10.1016/j.ccst.2023.100134. URL `https://linkinghub.elsevier.com/retrieve/pii/S2772656823000386`.

[25] Mohammad Jamali and Ahmad Azari. A review on computational fluid dynamics simulations of industrial amine absorber columns for CO_2 capture. *ChemBioEng Reviews*, 10(1):6–21, 2023. doi: 10.1002/cben.202200018.

[26] K. An, K. Li, C. M. Yang, J. Brechtl, D. Stamberga, M. Zhang, and K. Nawaz. Direct air capture with amino acid solvent: Operational optimization using a crossflow air-liquid contactor. *AIChE Journal*, e18429:1–11, 2024.

[27] Ugochukwu E. Aronu, Ardi Hartono, Karl A. Hoff, and Hallvard F. Svendsen. Kinetics of carbon dioxide absorption into aqueous amino acid salt: Potassium salt of sarcosine solution. *Industrial and Engineering Chemistry Research*, 50:10465–10475, 9 2011. ISSN 08885885. doi: 10.1021/ie200596y.

[28] Meng-Hui Li and Ming-Der Lai. Solubility and diffusivity of N_2O and CO_2 in (monoethanolamine + *N*-methyldiethanolamine + water) and in (monoethanolamine + 2-amino-2-methy 1-1-propanol + water). *Journal of Chemical Engineering Data*, 40:486–492, 1995. doi: 10.1021/je00018a029.

[29] Z. Wang, M. Gupta, S. S. Warudkar, K. R. Cox, G. J. Hirasaki, and M. S. Wong. Improved CO_2 absorption in a gas–liquid countercurrent column using a ceramic foam contactor. *Industrial Engineering Chemistry Research*, 55(5):1387–1400, 2016.

[30] Ralph Higbie. Penetration theory leads to use of the contact time in the calculation of the mass transfer coefficients in the two film theory. *Trans. Am. Inst. Chem. Engrs*, 31(365), 1935.

[31] John C. Lamont and D. S. Scott. An eddy cell model of mass transfer into the surface of a turbulent liquid. *AIChE Journal*, 16(4):513–519, 1970. doi: 10.1002/aic.690160403. URL `https://aiche.onlinelibrary.wiley.com/doi/abs/10.1002/aic.690160403`.

[32] Y W Wang, S Xu, F D Otto, and A E Mather. Solubility of N_2O in alkanolamines and in mixed solvents. *The Chemical Engineering Journal*, 48(1):31–40, 1992. doi: 10.1016/0300-9467(92)85004-S.

[33] Moon-Ki Park. Physical solubility of nitrous oxide in aqueous amine solutions. *Environmental Sciences Bulletin of The Korean Environmental Sciences Society*, 3(2):137–142, 1999.

[34] R. Sander. Compilation of Henry's law constants (version 4.0) for water as solvent. *Atmospheric Chemistry and Physics*, 15:4399–4981, 4 2015. ISSN 16807324. doi: 10.5194/acp-15-4399-2015.